Dalton Transactions

ROYAL SOCIETY OF CHEMISTRY

PAPER

View Article Online
View Journal | View Issue

Cite this: *Dalton Trans.*, 2026, **55**, 4181

Ligand decorated nickel-based nanoparticles supported onto MXenes in catalytic hydrogenation of N-heterocycles

Judith Medina-Vargas, [a] Santiago Martín, [b,c,d] Iván Sorribes, [a] Hermenegildo García *[a,e] and Jose A. Mata *[a]

The development of efficient first-row transition metal catalysts is essential for advancing sustainable chemical processes. In this study, we report the synthesis of nickel-based nanoparticles (NiNPs) functionalized with N-heterocyclic carbene ligands and immobilized onto **Ti_3C_2 MXene**. Our convergent synthetic approach enables comprehensive and straightforward characterization of each component within the final hybrid material. The NiNPs are obtained through chemical reduction of a well-defined nickel organometallic complex, resulting in the formation of small nickel metal nanoparticles (3.0 ± 0.8 nm) that are rapidly oxidized to the corresponding NiO and $Ni(OH)_2$ based nanoparticles containing surface NHC ligands. The hybrid catalyst exhibits high activity and selectivity in the hydrogenation of N-heterocycles under hydrogenation conditions, achieving quantitative yields at low catalyst loadings, particularly notable for a nickel-based system. Recycling studies revealed progressive catalyst deactivation, primarily due to sintering of NiNPs, which reduces the number of active surface sites. However, the catalytic activity can be fully restored through a mild regeneration treatment under reducing conditions. These findings underscore the potential of NiNP/MXene-based materials for selective hydrogenation reactions, and highlight the importance of addressing key challenges in sustainability such as the use of non-noble metals, catalyst stability and recyclability. Further design modifications aimed at preventing nanoparticle sintering may enhance the long-term viability of these systems in catalytic hydrogenation processes.

Received 17th November 2025,
Accepted 6th February 2026

DOI: 10.1039/d5dt02759d

rsc.li/dalton

Introduction

Nickel nanoparticles (NiNPs) have emerged as valuable components in heterogeneous catalysis owing to the natural abundance and low cost of nickel, as well as the distinctive electronic and structural features that enable fine control over their catalytic behavior.[1–5] Their catalytic versatility expands across a wide range of transformations including hydrogenation,[6–8] cross coupling reactions,[9–11] exchange processes,[12] reforming[13] and electrocatalysis.[14–16] The catalytic performance of NiNPs is strongly linked to surface stabilizers such as surfactants and ligands, as well as interactions with their supports.[17–19] The presence of surface modifiers confers stability and often induces selectivity,[20–23] while the support provides a structural matrix that prevents sintering and promotes the dispersion of nanoparticles, thereby increasing the number of accessible active sites.[24–28]

Traditional supports, including metal oxides (*e.g.*, Al_2O_3, SiO_2, and TiO_2), carbon-based materials (*e.g.*, graphene and derivatives, carbon nanotubes, and carbon nitride) and porous frameworks (*e.g.*, MOFs and zeolites) have provided valuable platforms for metal nanoparticle immobilization. However, the application of MXenes as a support for metal nanoparticles in thermal catalysis is still relatively underexplored. MXenes are a family of two-dimensional transition metal carbides and nitrides with the general formula $M_{n+1}X_n$ (M = early transition metal, X = C, N, n = 1–4).[29] MXenes are promising materials for diverse applications[30–33] including catalysis[34–42] and as support of metal nanoparticles where they offer a suitable 2D morphology and strong metal–support interactions.

Among catalytic transformations, the hydrogenation of quinolines and related N-heterocycles is of particular significance. These reactions are key steps in fine-chemical and pharmaceutical synthesis,[43–45] and play a pivotal role in liquid organic hydrogen carrier (LOHC) technology, where N-heterocycles act as reversible hydrogen storage media.[46–48] Developing nickel-based catalysts that combine high activity, selectivity, and

[a]*Institute of Advanced Materials (INAM), Universitat Jaume I, Avda. Sos Baynat s/n, 12071 Castellón, Spain. E-mail: jmata@uji.es*
[b]*Instituto de Nanociencia y Materiales de Aragón (INMA), CSIC-Universidad de Zaragoza, 50009 Zaragoza, Spain*
[c]*Departamento de Química Física, Universidad de Zaragoza, 50009 Zaragoza, Spain*
[d]*Laboratorio de Microscopias Avanzadas (LMA), Universidad de Zaragoza, Edificio I+D+i., 50018 Zaragoza, Spain*
[e]*Instituto de Tecnología Química, Consejo Superior de Investigaciones Científicas-Universitat Politècnica de València, Avda. Los Naranjos s/n, 46022 Valencia, Spain*

recyclability under mild conditions is therefore essential for sustainable hydrogenation chemistry.

In recent years, significant progress has been achieved in the development of nickel-based catalysts for the hydrogenation of N-heterocycles, with numerous systems demonstrating excellent activity (Table S1). For example, the transfer hydrogenation of quinolines using ammonia borane as a hydrogen source has been achieved under mild conditions (25 °C) employing Ni(II) complexes bearing amine ligands and nickel supported on carbonaceous materials.[49,50] Several nickel-based catalysts have also enabled quantitative hydrogenation of quinolines under molecular hydrogen at pressures of 20–30 bar and moderate temperatures (120 °C). However, most of these systems require relatively high metal loadings (≥4 mol%).[51–56] Moreover, along with the excellent activity of these materials, they also display good recyclability. However, the number of studies focusing on catalyst deactivation mechanisms and/or regeneration strategies remains scarce.

In contrast, the **NiNPs/NHC@MXene** hybrid catalyst developed in this work achieves 99% yield at moderate temperatures (120 °C, 30 bar H_2) with low Ni loading (3.7 mol%), maintaining recyclability and recoverable activity upon reductive regeneration. This performance compares favorably to state-of-the-art systems while employing a non-precious metal and a 2D support. The design of this hybrid system integrates N-heterocyclic carbene (NHC) ligands with the MXene surface and stabilizes nickel species during nanoparticle formation. The presence of the NHC ligand not only controls nanoparticle nucleation and morphology but also enhances electronic stabilization at the metal–support interface.

Herein, we report the synthesis of NiNPs functionalized with N-heterocyclic carbene (NHC) ligands anchored onto the **Ti_3C_2 MXene** through a convergent approach. The catalytic properties of this hybrid material in the hydrogenation of quinolines have been evaluated. Catalyst performance, substrate scope and recyclability have been determined, with particular attention to deactivation pathways and potential regeneration strategies. Our methodology enables the independent characterization of all components within the hybrid material and provides opportunities for tuning the active site, paving the way for the design of more effective catalysts in future studies.

Experimental

Materials and methods

The ligand precursor (bromide of methyl-methylpyrene-imidazolium salt) and the nickel–NHC complex (complex **1**) were synthesized according to previously reported procedures.[57,58] All reagents and solvents were used as received unless otherwise specified. Solvents were dried using a solvent purification system (SPS).

Nuclear magnetic resonance (NMR) spectra were recorded on Bruker spectrometers operating at 300 or 400 MHz (^{1}H NMR) and 75 or 100 MHz (^{13}C{^{1}H} NMR), respectively, and referenced to $SiMe_4$ (δ in ppm and J in Hz). NMR spectra were acquired at room temperature with the appropriate deuterated solvent.

Scanning electron microscopy (SEM) was performed using a JEOL 7001F microscope operating at 15 kV coupled with a Leica Zeiss LEO 440i system equipped with a 250 and 350 INCA (Oxford) software for the EDX analysis.

High-resolution transmission electron microscopy (HRTEM) images and high-angle annular dark-field images (HAADF-STEM) of the samples were acquired using a Jem-2100 LaB_6 (JEOL) transmission electron microscope coupled with an INCA Energy TEM 200 (Oxford) energy dispersive X-Ray spectrometer (EDX) operating at 200 kV. Sample preparation: a drop of the methanol-dispersed sample was deposited onto a carbon-coated copper grid and air-dried.

X-ray diffraction (XRD) patterns were recorded with a D8 Advance diffractometer from Bruker-AXS, with a Bragg–Brentano $\theta/2\theta$ geometry and Cu Ka radiation. The data were collected from 5° to 70°.

The nickel content in the hybrid material was determined by inductively coupled plasma mass spectrometry (ICP-MS). A 15 mg sample was digested using 69% nitric acid in a Mars 6 iWave microwave digestion system (CEM) under the following conditions: 1800 W power, 210 °C, and 25 minutes. After digestion, the sample was diluted to an appropriate volume (10 mL). ICP-MS measurements were performed in duplicate using an Agilent 7500 CX instrument.

X-ray photoelectron spectra (XPS) were acquired on a Kratos AXIS ultra-DLD spectrometer with a monochromatic Al Kα X-ray source (1486.6 eV) using a pass energy of 20 eV. All binding energies were calibrated with respect to the C 1s peak at 284.6 eV to ensure accurate referencing.

Gas chromatography (GC) analysis was performed on a Shimadzu GC-2010 apparatus equipped with a flame ionization detector (FID) and using a Teknokroma column (TRB-5MS; 30 m × 0.25 mm × 0.25 μm). Temperature program: (1) 80 °C, 10 °C min^{-1} until 150 °C, and 1 min. (2) 150 °C, 20 °C min^{-1} until 300 °C, and 2 min. Total time: 17.5 min (Fig. S1 & S2).

Hydrogen temperature programmed reduction (H_2-TPR) studies were carried out on a Micromeritics AutoChem apparatus (2910) connected to a thermal conductivity detector (TCD). Before the test, samples were pretreated under an Ar atmosphere at room temperature for 15 min. H_2-TPR analysis was carried out from 30 to 900 °C under a 10% H_2/Ar flow (50 mL min^{-1}) with a heating rate of 10 °C min.

Synthetic procedures

Synthesis of Ti_3C_2 MXene. The MXene support was synthesized by selectively etching the aluminum (Al) layer from the **Ti_3AlC_2 MAX phase**, using the method adapted from Gogotsi *et al.*'s study.[59,60] To a solution of 48% hydrofluoric acid (HF, 50 mL), Ti_3AlC_2 powder (5 g) was slowly added under stirring at room temperature. The mixture was stirred for 2 hours to allow complete etching. Afterward, the resulting black suspension was collected by centrifugation at 3500 rpm and washed with Milli Q water. The washing process was

repeated until the pH of the supernatant reached 5–6, indicating neutralization. Then, the resulting MXene ($Ti_3C_2T_x$) solid was collected and vacuum-dried at 80 °C for 24 hours. The final dry powder was stored in a glovebox under an inert atmosphere to prevent oxidation.

Synthesis of NiNPs/NHC@MXene. Ti_3C_2 powder (370 mg) was dispersed in a round-bottom flask with CH_2Cl_2 (40 mL) and sonicated for 30 minutes to ensure homogeneous suspension. Separately, 130 mg of complex **1** (Scheme S1) was dissolved in CH_2Cl_2 (20 mL) and then added to the Ti_3C_2 suspension. The resulting mixture was sonicated for an additional 5 minutes time. To induce the formation of nanoparticles, 1 equiv. of *tert*-butylamine borane adduct ($^tBuNH_2{\cdot}BH_3$), dissolved in 15 mL CH_2Cl_2, was added dropwise to the mixture under continuous stirring. The reaction mixture was then stirred at room temperature for 20 hours under a nitrogen atmosphere. After this time, the material was recovered by filtration, washed thoroughly with CH_2Cl_2 (3 × 5 mL), and dried under reduced pressure.

Synthesis of NiNPs@MXene. NiNPs lacking the NHC ligand were synthesized following a procedure analogous to that used for **NiNPs/NHCs@MXene** but employing water as the solvent and $Ni(NO_3)_2{\cdot}6H_2O$ as the nickel precursor. Specifically, Ti_3C_2 powder (70 mg) was dispersed in H_2O (10 mL), and a solution of $Ni(NO_3)_2{\cdot}6H_2O$ (15 mg) in H_2O (2 mL) was added. The reduction was carried out by the addition of one equivalent of $^tBuNH_2{\cdot}BH_3$, leading to the formation of NiNPs lacking the NHC ligand directly supported on the MXene surface.

Catalytic procedures and experiments

General procedure for hydrogenation of N-heterocycles. In a general catalytic experiment, a reaction vial (10 mL) equipped with a stirring bar was charged with 0.1 mmol of quinoline, 0.1 mmol of anisole, 30 mg of solid catalyst (corresponding to 3.7 mol% of Ni surface atoms) and 2 mL of solvent. The vial was placed inside a stainless-steel autoclave. The reactor was sealed, purged 3 times with hydrogen (10 bar), then pressurized to 30 bars of H_2 and heated at 120 °C for 17 hours under continuous stirring. After the reaction time, the autoclave was allowed to cool to room temperature and slowly depressurized. Reaction yields and conversions were determined by GC-FID and/or ^1H NMR analysis using 1,3,5-trimethoxybenzene as an internal standard.

Recycling experiments. After performing a general catalytic experiment, the solid catalyst Ni-NPs/NHC@MXene was recovered by filtration and washed thoroughly with ethanol (3 × 5 mL) to remove residual reactants and products. The washed catalyst was dried under vacuum and reused directly in a subsequent catalytic run without any regeneration or activation treatment. Reaction evolution was evaluated using the general procedure described in the catalytic experiments.

Catalyst regeneration. The used catalyst was recovered by filtration and washed with ethanol (3 × 5 mL). Then, the solid catalyst was suspended in CH_2Cl_2 and sonicated for 30 minutes to ensure appropriate dispersion. Subsequently, two equivalents of $^tBuNH_2{\cdot}BH_3$, with respect to the Ni content, were added to the mixture, and the suspension was stirred at room temperature overnight (20 hours). After completion of the regeneration process, the catalyst was isolated by filtration, washed with CH_2Cl_2 (3 × 5 mL), and dried under reduced pressure. The regenerated catalyst was stored under nitrogen until further use.

Results and discussion

Synthesis and characterization

NiNPs decorated with NHCs supported on **Ti_3C_2 MXene** were synthesized *via* a convergent approach (Fig. 1). **Ti_3C_2 MXene** nanosheets were first prepared by etching the Al layer of the **Ti_3AlC_2 MAX phase** using HF. In parallel, the nickel complex **1** was synthesized *via* metallation of an NHC ligand precursor containing a pyrene moiety (Scheme S1). This NHC-pyrene ligand was selected based on prior studies demonstrating its effectiveness in anchoring metal complexes onto 2D materials[61–63] and its role in stabilizing metal nanoparticles

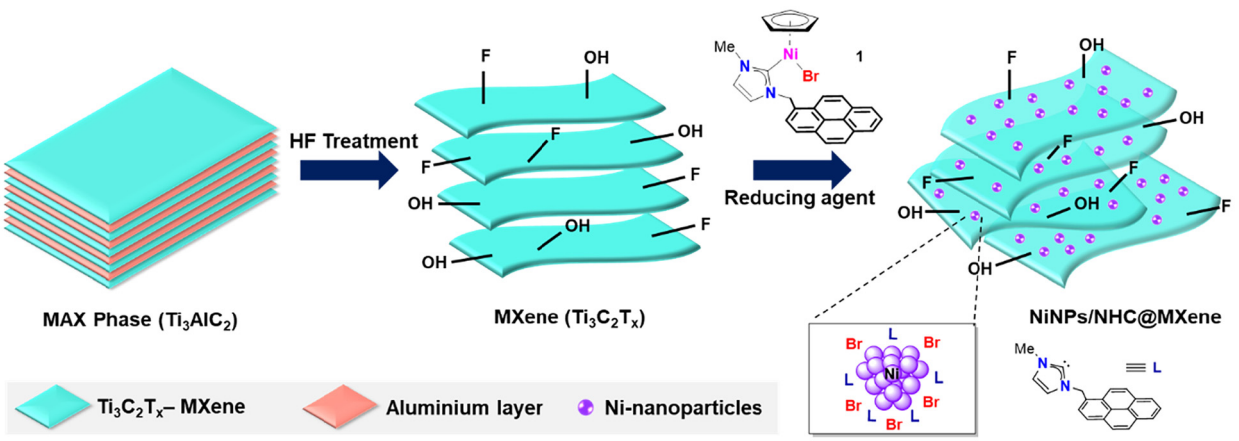

Fig. 1 Synthesis of NiNPs functionalized with NHC carbene ligands supported onto MXene.

(Fig. S3 & S4).[45,64–66] Metal complex **1** was then chemically reduced in a controlled manner using $^{t}BuNH_2{\cdot}BH_3$, resulting in the formation of NiNPs. These NiNPs, stabilized by NHC ligands, were *in situ* supported on the MXene surface, yielding the hybrid material **NiNPs/NHC@MXene**. This convergent synthetic strategy enables rational and precise control over the material formation, while also facilitating the characterization of both the MXene support and the active catalytic site.

The **Ti_3AlC_2 MAX phase**, **Ti_3C2 MXene** and MXene decorated with NiNPs (**NiNPs/NHC@MXene**), and the corresponding nickel complex were characterized using different microscopic, spectroscopic and analytical techniques. Detailed experimental procedures and additional materials are provided in the SI. Systematic characterization at each stage of synthesis enables a comprehensive understanding of the material properties and the structural and compositional changes occurring throughout the synthetic process.

Morphological analysis of **Ti_3C_2 MXene** *via* SEM microscopy confirms the successful removal of the aluminum layer from the parent Ti_3AlC_2 (Fig. 2a). The initially compact laminar structure of Ti_3AlC_2 is transformed into a characteristic accordion-like morphology using HF (Fig. 2b). This morphological change provides direct evidence of the success of the etching procedure (Fig. S5–S7). This structural change is further corroborated by EDX analysis (Fig. S8). Comparison of the EDX analysis results of the MAX and MXene samples reveals a significant reduction in aluminum content and the appearance of fluorine on the MXene sample. The microscopic characterization of **NiNPs/NHC@MXene** required the use of HRTEM to observe the presence of NiNPs due to a low contrast and small size of the NiNPs. Despite these challenges, HRTEM images clearly confirm the formation of spherical NiNPs uniformly distributed on the MXene surface (Fig. 2c). Size distribution analysis was performed by analyzing *ca.* 200 NiNPs from different HRTEM images. The results indicate an average particle diameter of 3.0 ± 0.8 nm, with a relatively narrow distribution (Fig. 2d). EDX analysis further confirmed nickel as a major component in the nanoparticles (Fig. S9 & S10).

Further evidence in the transformation of the **Ti_3AlC_2 MAX phase** into the **Ti_3C_2 MXene** and the successful incorporation of NiNPs to form **NiNPs/NHC@MXene** was obtained through comparative powder X-ray diffraction analysis (XRD) (Fig. 3). The **Ti_3AlC_2 MAX phase** exhibits sharp reflections of the hexagonal phase (space group $P6_3/mmc$) at 10°, 19° and 39° with Miller indices (002), (004) and (104), respectively (JCPDS 52-0875). These peaks are characteristic of the **Ti_3AlC_2 MAX phase**. The high crystallinity and narrow peaks indicate a well-ordered layered structure composed of Ti–C octahedral slabs interleaved with Al atomic layers.[67] In contrast, the **Ti_3C_2 MXene** displays broad low-intensity peaks, characteristic of its lamellar structure and reduced crystallinity. A key distinction between the **Ti_3C_2 MXene** and the parent **Ti_3AlC_2 MAX phase** is the shift of the (002) peak to lower angles (from 10° to 7.5°), attributed to the removal of aluminum atoms. Additionally, the disappearance of the (104) peak at 39° confirms the complete elimination of the aluminum layer and verifies the formation of a pure **Ti_3C_2 MXene phase**.

The presence of NiNPs does not disturb the XRD pattern of the **Ti_3C_2 MXene**. A slight shift of the (002) peak of **Ti_3C_2 MXene** towards lower angles is observed (from 7.5° to 6.8°), indicating an increase in interlayer spacing which supports the insertion of NiNPs into the MXene layers. However, no distinct peaks corresponding to nickel-based nanoparticles (Ni metal,

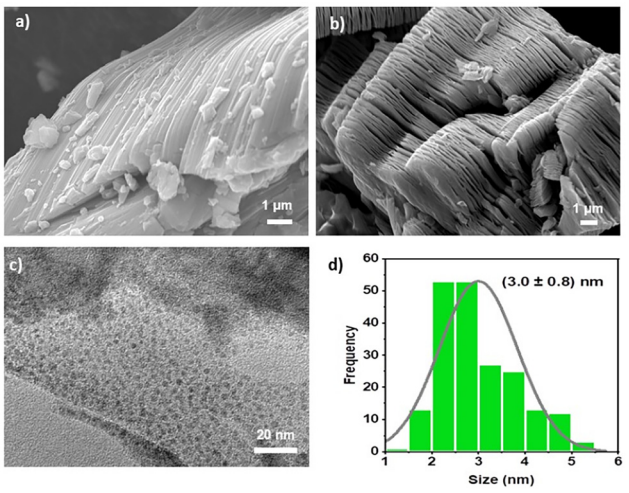

Fig. 2 Morphological characterization. (a) SEM image of the **Ti_3AlC_2 MAX phase**. (b) SEM image of **Ti_3C_2 MXene**. (c) HRTEM image of **NiNPs/NHC@MXene** and (d) size histogram of **NiNPs/NHC@MXene** (N = 200).

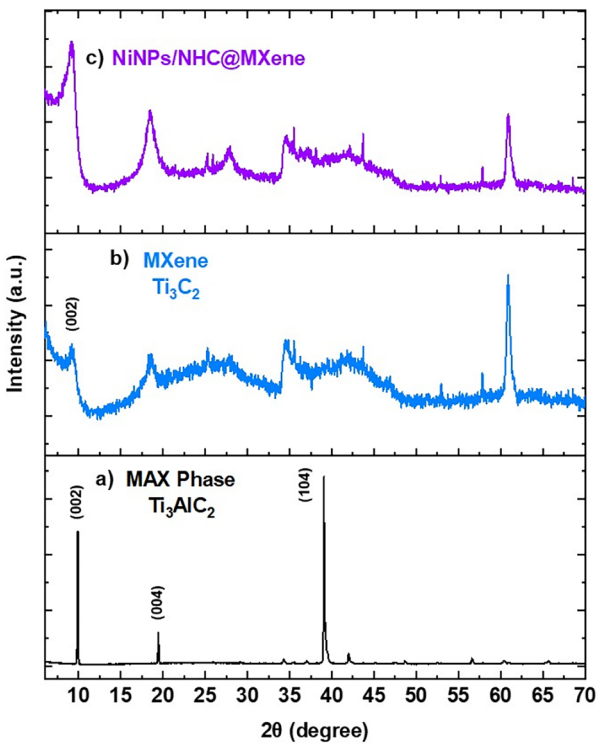

Fig. 3 Comparative XRD of the **Ti_3AlC_2 MAX phase** (a), **Ti_3C_2 MXene** (b) and **NiNPs/NHC@MXene** (c).

NiO and/or $Ni(OH)_2$) are detected, probably due to their low concentration of nickel relative to the **Ti_3C_2 MXene** matrix (1/25 ratio in weight).

X-ray diffraction analysis confirms the transformation of the **Ti_3AlC_2 MAX phase** to the **Ti_3C_2 MXene** and provides indirect evidence on the intercallation of nickel-based nanoparticles into the MXene structure; however, this does not confirm the exact nature (Ni, NiO or $Ni(OH)_2$) of these nickel-based nanoparticles.

Further insights into the chemical composition and oxidation states of elements in the hybrid material **NiNPs/NHC@MXene** were obtained by X-Ray Photoelectron Spectroscopy (XPS). The survey spectrum of MXene confirms the presence of Ti, C, O and F along with the disappearance of the Al signal observed in the **Ti_3AlC_2 MAX phase** (Fig. 4), clearly indicating the successful etching of the aluminum layer using HF. The high-resolution XPS spectrum peak of Ti 2p in Ti_3C_2 was deconvoluted into components corresponding to Ti–C, C–Ti–F and C–Ti–O (model shown in Fig. 5). The Ti–C component originates from the titanium-carbon bonds within the internal layers of MXene, while the C–Ti–F and C–Ti–O peaks confirm surface functionalization resulting from the etching process (Fig. 4).[68]

Analysis of the high-resolution XPS C 1s spectrum supports the carbide nature of the material. The deconvoluted peaks at 281.9 eV and 283.2 eV are assigned to C–Ti bonding environments within the internal layers of the MXene. Peaks corresponding to C–T (T = F, O, OH) surface terminations are barely detectable due to their low relative abundance. A dominant graphitic C–C peak is observed at 284.6 eV, along with a small C–O peak at 286.1 eV, likely arising from partial oxidation by atmospheric oxygen.[69,70]

The high-resolution XPS data of the O 1s region reveal the presence of surface terminal oxygen atoms bonded to titanium. Additionally, the O_{fcc} component, indicative of oxygen atoms on the face-centered cubic (fcc) lattice sites, is typically associated with well-ordered metal oxides such as Al_2O_3 and TiO_2 and may represent residual oxide impurities.[71] Further details of XPS analysis can be found in the SI (Fig. S11 and S12).

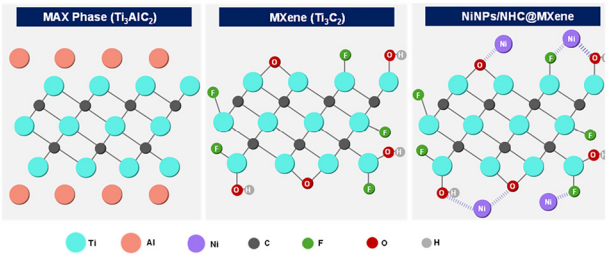

Fig. 5 Model structures of the **Ti_3AlC_2 MAX phase**, **Ti_3C_2 MXene** and the **NiNPs/NHC@MXene** showing the main contributions observed by XPS analysis.

XPS characterization was also performed on the **NiNPs/NHC@MXene material** (Fig. 6). The corresponding survey spectra and additional XPS details are provided in the SI (Fig. S13). The survey spectrum of the as-prepared material reveals the presence of titanium, nickel, carbon, nitrogen, fluorine, bromine, and oxygen species, verifying the coexistence of the MXene support, nickel-base nanoparticles, and nitrogen-containing NHC ligands. In the Ti 2p region, distinct peaks corresponding to Ti–C (Ti $2p_3/_2$ at 454.5 eV) confirm the retention of the carbide structure of **Ti_3C_2**. Additional components at 456.0, 457.6, 460.1, 461.3, and 462.3 eV are attributed to Ti^{2+}, Ti–O_2, and higher oxidation state Ti^{3+}/Ti^{4+}, indicative of partial surface oxidation of Ti atoms during etching and post-synthesis air exposure. This is a common feature in MXenes, where surface Ti atoms readily form terminal –O and –OH groups. The Ti 2p spectrum of the **NiNPs/NHC@MXene** material shows similar components to the parent **Ti_3C_2 MXene**. The high-resolution Ni 2p core-level spectrum shows characteristic peaks at 856.4 eV and 859.3 eV in the Ni $2p_{3/2}$

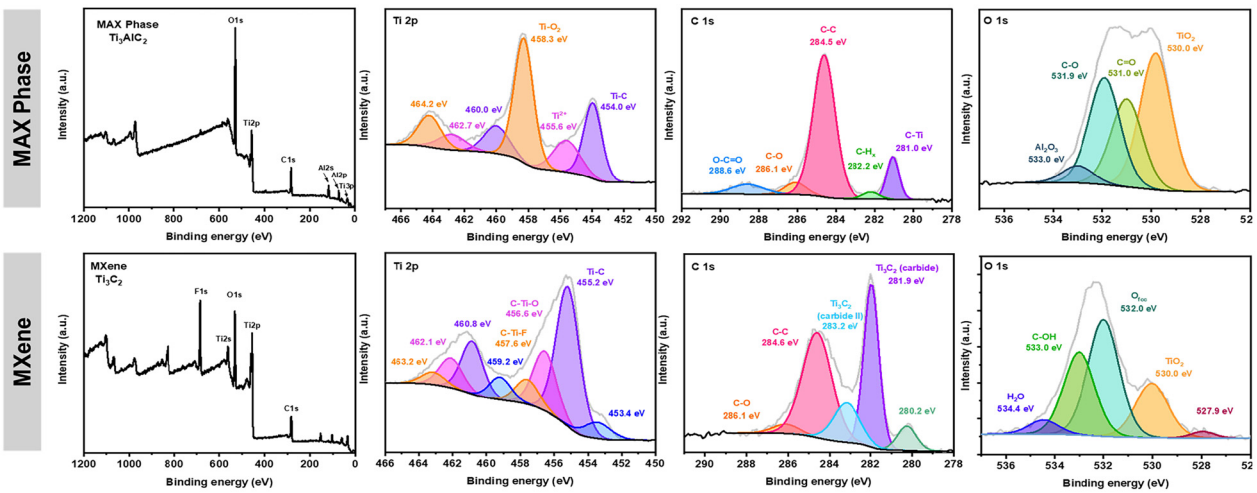

Fig. 4 Comparative XPS analysis of the **Ti_3AlC_2 MAX phase** *vs.* the **Ti_3C_2 MXene**. Survey spectrum and high-resolution core-level peaks corresponding to Ti 2p, C 1s and O 1s.

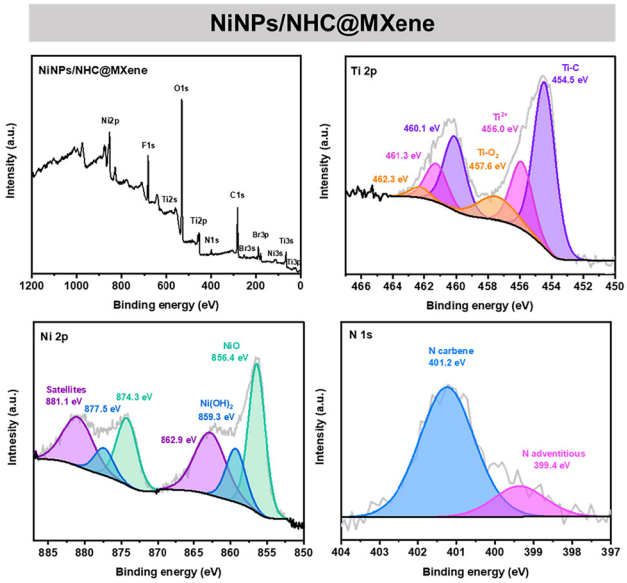

Fig. 6 XPS analysis of **NiNPs/NHC@MXene**. Survey spectrum and high-resolution core-level peaks corresponding to Ti 2p, N 1s and Ni 2p.

region, corresponding to Ni–O and Ni–OH, respectively. The 856.4 eV peak may also indicate Ni–F bonding, which can arise from interactions between the nickel- and fluorine-terminated MXene surface. These interactions likely result from functional groups (O, OH, and F) formed on the MXene surface during the etching process and contribute to the stabilization of nickel species. The satellite Ni peaks are observed at 862.9 eV (Ni $2p_{3/2}$) and 881.1 eV (Ni $2p_{1/2}$), further confirming the oxidized state of nickel species. The absence of a distinct metallic Ni^0 peak around 852.6 eV suggests that the surface of the Ni nanoparticles is largely oxidized to $NiO/Ni(OH)_2$ under ambient conditions. The XPS provides surface information of the top few nanometers (penetration depth: 7–10 nm), and it could be argued that the nanoparticles could retain a metallic Ni core beneath this oxidized shell. However, this behavior is not expected in the NiNPs anchored on **Ti_3C_2 MXene** due to the small size of the nanoparticles (3.0 ± 0.8 nm).[72–74] In the N 1s region, a prominent peak at 401.2 eV corresponds to carbene-type nitrogen from the NHC ligand bound to the Ni surface, evidencing its presence in the hybrid material. A secondary peak at 399.4 eV is assigned to adventitious or pyridinic nitrogen, likely arising from trace adsorbates.

These features collectively confirm the successful anchoring of Ni nanoparticles functionalized with NHC ligands on the **Ti_3C_2 MXene** surface. The nature of these NiNPs is consistent with a $NiO/Ni(OH)_2$ species containing NHC ligands.

Catalytic properties

Catalytic studies were initiated by optimizing the reaction conditions for the hydrogenation of quinoline (**1D**), selected as the model substrate. The reaction conditions were systematically optimized by varying key parameters, including the individual components of the hybrid catalytic material, temperature, hydrogen pressure and solvent. Control experiments conducted without any catalyst or using the **Ti_3AlC_2 MAX phase** or the **Ti_3C_2 MXene** alone demonstrated that these systems are not active in the hydrogenation of quinoline (**1D**) (Table 1, entries 1–3). In contrast, the hydrogenation of quinoline (**1D**) under homogeneous conditions using complex **1** provided 60% yield of the corresponding tetrahydroquinoline (entry 4). These control experiments confirm nickel as the primary active catalytic species in the hydrogenation of quinolines.

We then studied the influence of the NHC ligand in the catalytic performance of the hybrid material. In a first set of experiments, a direct comparison required the preparation of analogous NiNPs supported on MXene, but without the NHC ligand. To achieve this, we followed the same synthetic protocol used for **NiNPs/NHC@MXene**, replacing the organometallic complex **1** with $Ni(NO_3)_2{\cdot}6H_2O$ as the nickel source. This procedure resulted in the formation of NiNPs supported on MXene, designated as **NiNPs/MXene**, lacking the NHC ligand. Characterization by HRTEM microscopy revealed the formation of prismatic nanoobjects (Fig. S14 & S15). The particle size distribution of **NiNPs/MXene** was more challenging due to the less well-defined morphology. Nevertheless the average particle diameter was estimated to be approximately 4.1 nm (N = 100), which is comparable to that of **NiNPs/NHC@MXene** (3.0 nm) (Fig. S16). The different morphology obtained using different nickel sources confirmed the role of the NHC ligand in the formation/nucleation of NiNPs. The catalytic activity of **NiNPs/MXene** was then evaluated in the hydrogenation of quinoline (**1D**) under standard conditions. Notably, the material exhibited negligible catalytic activity (Table 1, entry 5). This result underscores the critical role of the NHC ligand in maintaining the activity and stability of the NiNPs.

We then explored the catalytic performance of NiNPs supported on MXene using an alternative NHC ligand with different structural properties (Me_2NHC). We followed the same preparation method as for **NiNPs/NHC@MXene**. We synthesized complex **2** using the ligand Me_2NHC and reduced with ^{t}BuNH$_2{\cdot}$BH$_3$ to generate the new hybrid material, **NiNPs/Me_2NHC@MXene**. Experimental details of synthetic procedures and characterization data are provided in the SI (section S9, Fig. S17–S21). HRTEM analysis revealed spherical NiNPs with an average diameter of 4.7 ± 2.4 nm. These NiNPs are relatively larger and more broadly distributed than those in **NiNPs/NHC@MXene** (3.0 ± 0.8 nm). Catalytic evaluation of complex **2** under homogeneous conditions showed lower activity than complex **1** (Table 1, entry 6), whereas the hybrid material **NiNPs/Me_2NHC@MXene** exhibited catalytic performance comparable to that of **NiNPs/NHC@MXene** (Table 1, entry 7). These findings indicate that, although the NHC ligand plays a key role in nanoparticle formation, the subtle structural variations in the ligand have only a modest influence on the overall catalytic activity.

Hydrogenation of quinoline (**1D**) using the NiNPs containing the NHC ligand, **NiNPs/NHC@MXene**, under the standard conditions resulted in a 95% yield of tetrahydroquinoline (**1H**)

Table 1 Reaction optimization using quinoline as a model substrate

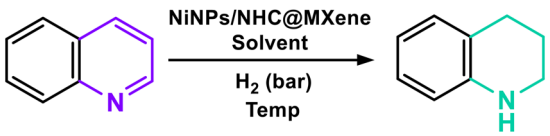

Entry	Cat.	Solvent	Temp. (°C)	P_{H_2} (bar)	Conv.[a] (%)	Yield[b] (%)
1	—	EtOH	150	30	0	0
2	**Ti_3AlC_2 MAX phase**[c]	EtOH	150	30	1	0
3	**Ti_3C_2 MXene**[c]	EtOH	150	30	3	2
4	Complex **1**[d]	EtOH	150	30	63	60
5	**NiNPs@MXene**	EtOH	150	30	5	5
6	Complex **2**[d]	EtOH	150	30	35	33
7	**NiNPs/Me_2NHC@MXene**	EtOH	150	30	94	90
8	**NiNPs/NHC@MXene**	EtOH	150	30	96	95
9	**NiNPs/NHC@MXene**	EtOH	120	30	99	98
10	**NiNPs/NHC@MXene**	EtOH	100	30	27	12
11	**NiNPs/NHC@MXene**	EtOH	70	30	3	0
12	**NiNPs/NHC@MXene**	EtOH	120	20	56	41
13	**NiNPs/NHC@MXene**	EtOH	120	6	9	7
14	**NiNPs/NHC@MXene**	EtOH	120	1	3	3
15	**NiNPs/NHC@MXene**	MeOH	120	30	98	91
16	**NiNPs/NHC@MXene**	2-PrOH	120	30	95	94
17	**NiNPs/NHC@MXene**	Toluene	120	30	4	1
18	**NiNPs/NHC@MXene**	1,4-Dioxane	120	30	6	0
19	**NiNPs/NHC@MXene**	*o*-DCB	120	30	7	4
20	**NiNPs/NHC@MXene**	*p*-Xylene	120	30	0	0
21	**NiNPs/NHC@MXene**	*o*-Xylene	120	30	0	0
22	**NiNPs/NHC@MXene**	Hexane	120	30	7	6

General reaction conditions: quinoline (**1D**) (0.1 mmol); catalyst loading (3.7 mol% based on Ni_{surf}); and solvent (2 mL). [a] Conversion calculated by GC/FID using anisole as an internal standard. [b] Yield calculated by ^{1}H NMR spectroscopy using 1,3,5-trimethoxybenzene as an external standard. [c] Catalyst loading: 20 mg. [d] Catalyst loading: 3.7 mol%.

(Table 1, entry 8). Temperature screening revealed that diminishing the reaction temperature from 150 °C to 120 °C maintained product formation within the quantitative range (Table 1, entry 9), while further decrease to 100 °C or below significantly reduced the yield (Table 1, entries 10–12). Different hydrogen pressures were tested to identify the most efficient one; however decreasing hydrogen pressure below 30 bar provided lower yields (Table 1, entries 12–14). A range of solvents were scrutinized to determine their influence on the hydrogenation of quinoline (**1D**) (Table 1, entries 15–22). Among them, alcohols provided the highest yields using either methanol or isopropanol as an alternative to ethanol. In contrast, other solvents gave poor results, indicating that solvent polarity plays a crucial role, likely due to enhanced charge separation in the transition state. The hydrogenation reactions were performed using a catalyst loading of 3.7 mol% nickel, calculated based on the dispersion factor that accounts exclusively for nickel atoms located on the surface of the nanoparticles. The number of surface-exposed nickel atoms was estimated under the assumption of a spherical nanoparticle morphology. Details of the calculation procedure are provided in the SI (Table S2).

Based on the systematic optimization studies, the optimal reaction conditions were identified as 120 °C, 30 bar hydrogen pressure and ethanol as solvent, resulting in a 98% yield using a catalyst loading of 3.7 mol% of nickel. With the optimal conditions, we screened the overall reaction trend by monitoring product formation and reagent disappearance by GC/FID until completion (Fig. 7). The reaction progress was monitored over time, showing a steady increase in the concentration of tetrahydroquinoline (**1H**) concurrent with a steady decrease in the concentration of quinoline (**1D**). The mass balance indicates

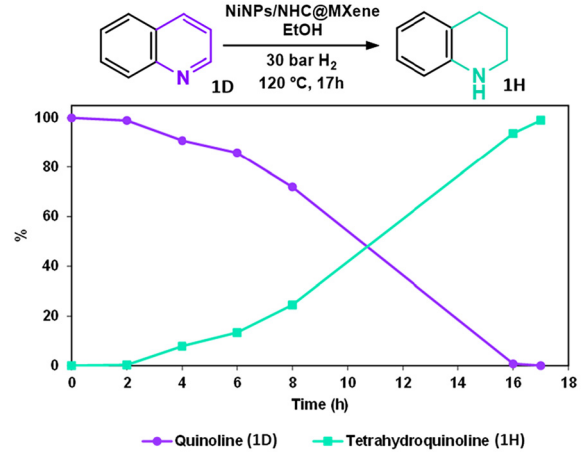

Fig. 7 Reaction monitoring in the hydrogenation of quinoline (**1D**). Conditions: quinoline (0.1 mmol), catalyst loading (3.7 mol% based on Ni_{surf}), 130 °C, 30 bar H_2 and EtOH (2 mL).

the complete conversion of the reagent into the product without detectable formation of side products. These results confirm the high activity and selectivity of the **NiNPs/NHC@MXene** catalyst in the hydrogenation of quinoline (**1D**).

To evaluate the generality and limitations of the hydrogenation of N-heterocycles catalyzed by **NiNPs/NHC@MXene**, the substrate scope under the optimized conditions previously established was investigated. A range of substrates bearing various functional groups at different positions on the heterocyclic ring were tested. The reaction progress was independently assessed by monitoring substrate conversion and product yield. Conversion was determined by GC/FID using anisole as an internal standard, while the product yield was quantified by ^{1}H NMR spectroscopy using 1,3,5-trimethoxybenzene as an external standard (Table 2).

The catalytic material **NiNPs/NHC@MXene** is active across a series of N-heterocycles, providing good to excellent yields regardless of the electronic nature or position of substituents (Table S3). Quinoline (**1D**) and its methyl-substituted derivatives at the 2- (**2D**), 6- (**3D**), or 8- (**4D**) positions were hydrogenated quantitatively (Table 2, entries 1–4). A bulky substituent at the 6-position did not significantly impact the yield (**5D**); however, a phenyl group at the 2-position (**6D**) resulted in reduced catalytic efficiency, yielding a lower conversion (Table 2, entries 5 and 6). The presence of electron-donating (MeO–) (**8D**) and electron-withdrawing (Cl– or CF_3^-) (**7D** and **9D**) groups at the six position of the aromatic ring do not affect the reaction outcomes affording quantitative yields in all cases (Table 2, entries 7–9). Notably, more sterically or electronically complex substrates such as isoquinoline (**10D**) and benzo[*h*]quinoline (**11D**) also underwent successful hydrogenation, albeit with lower yields (53% and 57%, respectively) under the standard reaction conditions, likely due to slower reaction kinetics (Table 2, entries 10 and 11). Throughout the substrate scope study, no side products were detected. Only starting materials and the fully hydrogenated N-heterocycles were observed, as confirmed by ^{1}H NMR analysis of the crude reaction mixtures (Fig. S22–S32), highlighting the high selectivity of the catalytic system. These results demonstrate that NiNPs functionalized with N-heterocyclic carbene ligands and supported on MXene represent an efficient and selective catalytic platform for the hydrogenation of N-heterocycles.

Table 2 Reaction scope in the hydrogenation of quinolines to tetrahydroquinolines

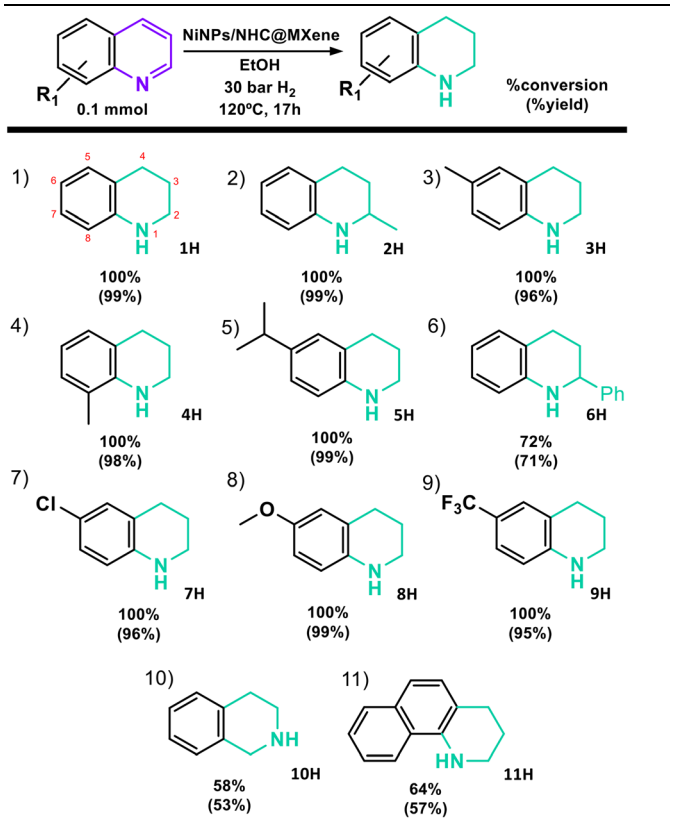

Reaction conditions: substrate (0.1 mmol), catalyst loading (3.7 mol% based on Ni_{surf}), 120 °C, and EtOH (2 mL). Conversion calculated by GC/FID using anisole as an internal standard. Yield calculated by ^{1}H NMR using 1,3,5-trimethoxybenzene as an external standard. D and H correspond to dehydrogenated and hydrogenated versions of the same compound, respectively.

Recycling and reusability experiments

The reusability of **NiNPs/NHC@MXene** was evaluated through recycling experiments, in which the catalyst performance for quinoline (**1D**) hydrogenation was evaluated under identical reaction conditions across successive runs (Fig. 8). After each cycle, the solid catalyst was recovered by filtration, washed with EtOH (3 × 5 mL), air-dried, and reused in a new reaction with fresh reagents and solvent. The results showed that the catalytic performance of **NiNPs/NHC@MXene** rapidly decreased, going from 98% yield in the first run to a 21% yield in the fourth run. Catalyst deactivation is a major challenge in catalysis, often limiting efficiency and increasing operational costs. To investigate the deactivation mechanism and explore pathways for catalyst improvement, the spent catalyst was analyzed using XRD analysis and microscopic techniques to ident-

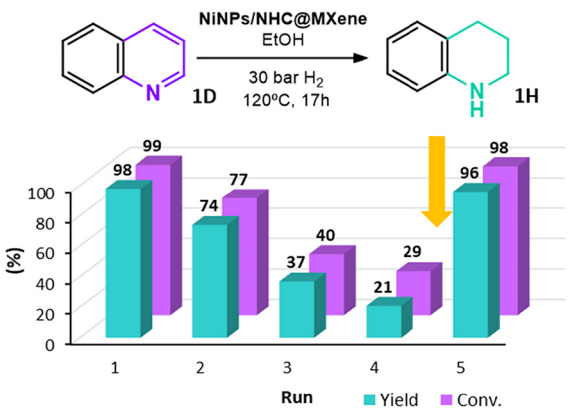

Fig. 8 Recycling and reusability properties of **NiNPs/NHC@MXene**. The yellow arrow indicates catalyst regeneration.

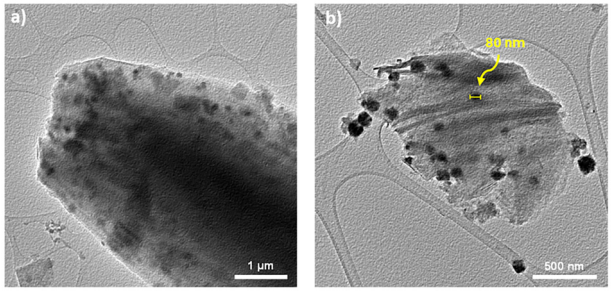

Fig. 9 HRTEM characterization of **NiNPs/NHC@MXene** after 4 catalytic cycles at 1 µm (a) and 500 nm (b).

ify changes in the support and the active metal species. First, the morphology of the spent catalyst was analyzed by microscopy. HRTEM revealed a notable morphological transformation: while the freshly prepared **NiNPs/NHC@MXene** contained NiNPs averaging 3 nm in size (Fig. 2d), after four catalytic runs, the average size increased dramatically up to 80 nm (Fig. 9). Morphological analysis suggests that nanoparticle sintering is a major contributor to catalyst deactivation.

The surface chemical composition and oxidation states of the **NiNPs/NHC@MXene** catalyst were analyzed by XPS before and after consecutive catalytic cycles (Fig. 10 and S33, S34). The as-prepared sample exhibits characteristic Ti 2p, Ni 2p, and C 1s signals consistent with **Ti_3C_2 MXene** decorated with Ni-based nanoparticles as previously described. In the Ti 2p region, the peaks at 454.5 eV and 456.0 eV correspond to Ti–C and Ti^{2+} species, respectively, whereas signals at 457.6–462.3 eV are attributed to surface Ti–O_x species (TiO_2 and other oxides). These features remain nearly unchanged after the first catalytic run, indicating a certain stability of the MXene support under the reaction conditions. However, after the fourth run, there is a clear increase in the intensity of the peak attributed to surface Ti–O_x species, suggesting progressive surface oxidation of the MXene.

The Ni 2p spectra of the as-prepared material show a main component as a doublet peak at 856.4 eV (Ni $2p_{3/2}$) and 874.3 eV (Ni $2p_{1/2}$) corresponding to NiO, along with their characteristic satellite features. The intensity of this NiO component gradually decreases in favor of the $Ni(OH)_2$ species, and this transformation is evident after the first catalytic run. Following four catalytic cycles, the Ni 2p region is dominated by the doublet peak of $Ni(OH)_2$ at 859.3 and 877.9 eV, evidencing the formation of hydroxylated nickel species. The C 1s spectra display a dominant C–C peak at 284.5 eV, with additional components assigned to C–O (286.1 eV), C=O (287.9 eV), and Ti–C (281.1 eV). The persistence of the Ti–C signal confirms the retention of the MXene carbide structure after the four catalytic runs. A clear increase in oxygenated carbon species is observed after successive runs as evidenced by the intensified C–O signal at 286.2 eV, which is attributed to surface oxidation. In the N 1s region, the peak at 401.2 eV, corresponding to carbene-type nitrogen from the NHC ligand, is clearly observed after the first catalytic run (Fig. S33). However, this signal is no longer visible after four catalytic cycles, suggesting that the NHC ligand detaches from the NiNP surface during repeated reactions (Fig. S34). These results indicate that the NHC ligand remains partially present after the first catalytic cycle but is completely lost after four cycles.

Overall, the XPS analysis during reusability experiments confirmed a higher oxidation degree of the **NiNPs/NHC@MXene** catalyst. Although catalytic reactions occur under reducing conditions, the observed oxidation likely results from the formation of highly reactive Ni surface sites during hydrogenation that subsequently oxidize upon exposure to air after each reaction cycle.

To further elucidate the redox behavior of NiNPs on MXene we performed H_2 temperature programmed reduction (H_2-TPR) analysis of the support **Ti_3C_2 MXene**, the as-prepared **NiNPs/NHC@MXene** catalyst and the corresponding used catalyst (Fig. 11). The H_2-TPR profile of **Ti_3C_2 MXene** exhibits only weak hydrogen consumption below 400 °C and a broad high-temperature reduction feature above 700 °C, which can be attributed to stable Ti–O species, confirming the absence of readily reducible surface species under typical hydrogenation conditions.[75] Upon deposition of nickel nanoparticles, a new and well-defined reduction peak appears at approximately 340 °C, which is assigned to the reduction of oxidized nickel species ($NiO/Ni(OH)_2$). This behaviour indicates the presence of finely dispersed and readily reducible Ni nanoparticles on the MXene surface, in agreement with HRTEM analysis results (Fig. 2c & d). After catalytic hydrogenation, the TPR profile retains a nickel-related reduction feature at a similar temperature, although slightly shifted and narrowed, suggesting changes in nanoparticle dispersion consistent with partial sintering during catalysis. This interpretation is further supported by HRTEM analysis of the used catalyst (Fig. 9). Importantly, the high-temperature reduction feature associated with the MXene support remains essentially unchanged, demonstrating that the Ti_3C_2 framework is structurally stable under the applied reaction conditions. Given that the hydrogenation reactions are performed under significantly more reducing conditions (30 bar H_2 at 120 °C for several hours) than those employed during H_2-TPR measurements, it is reasonable to infer that $NiO/Ni(OH)_2$ species are at least partially, and likely predominantly, reduced to metallic Ni during catalysis. This interpretation is consistent with the observed catalytic activity and with literature reports identifying Ni^0 as the active phase in nickel-catalyzed hydrogenation reactions.[76–78]

Overall, the H_2-TPR results indicate that catalyst deactivation is primarily related to nanoparticle agglomeration rather than irreversible oxidation of either the nickel species or the MXene support.

To address the observed deactivation, a regeneration strategy was explored involving a reductive treatment aimed at restoring nanoparticle dispersion. The spent catalyst was treated with ^{t}BuNH$_2$·BH$_3$ under stirring for 20 hours, following the same procedure used for the as-prepared catalyst. This treatment successfully recovered the catalytic performance to

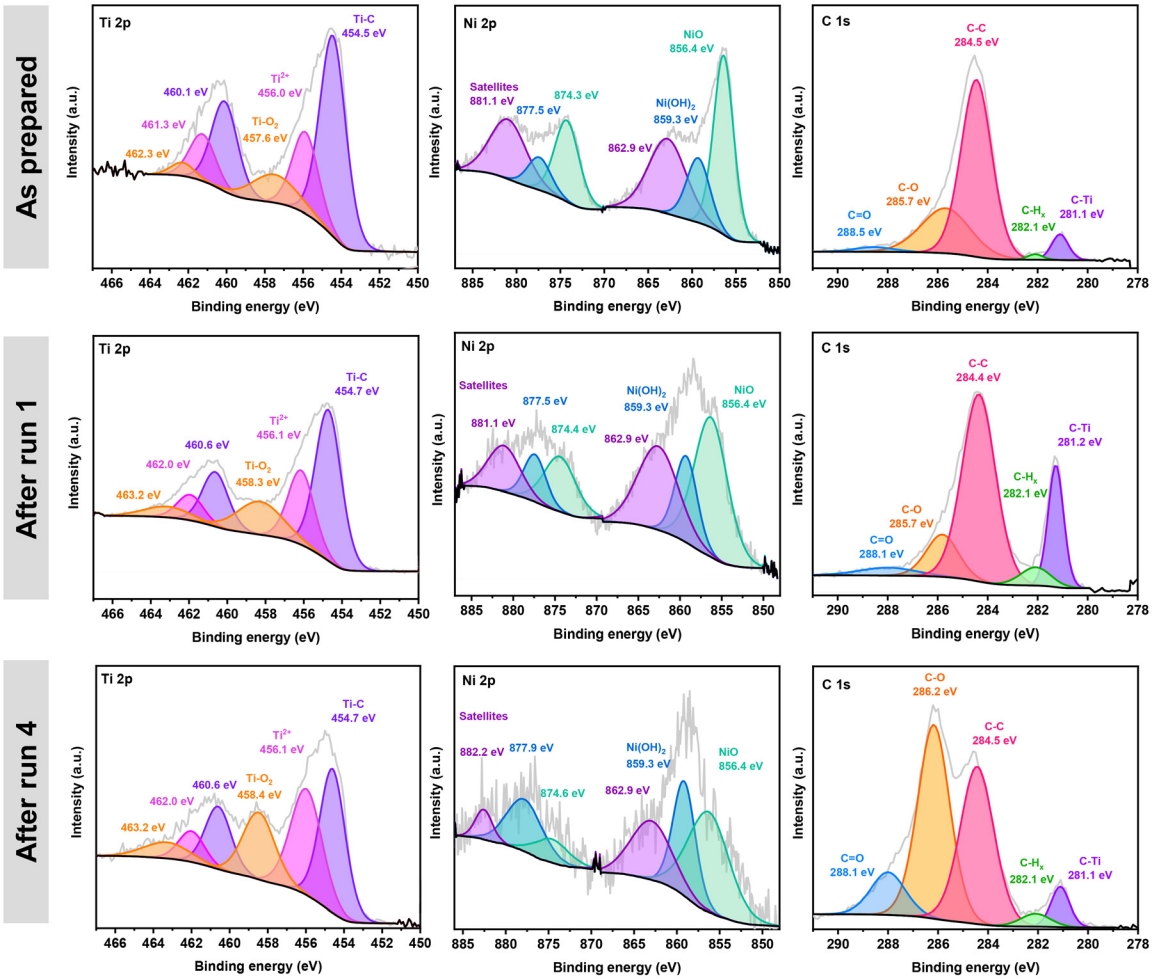

Fig. 10 Comparative XPS characterization of the **NiNPs/NHC@MXene** initial material and during the recycling experiments. High resolution core-level peaks corresponding to Ti 2p, Ni 2p and C 1s.

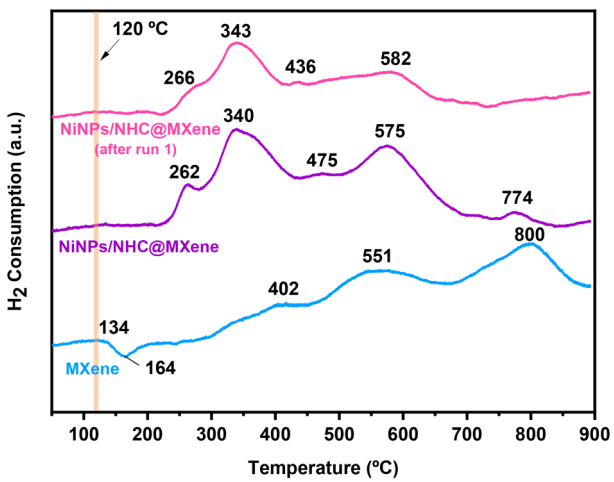

Fig. 11 H_2-TPR profiles of Ti_3C_2 **MXene** and the as-prepared and used **NiNPs/NHC@MXene** catalyst.

its initial level (Fig. 8, run 5). Further evidence of the successful regeneration process was experimentally obtained by XRD (Fig. 12). The characteristic diffraction peaks of **NiNPs/NHC@MXene** gradually broadened and eventually disappeared after four catalytic runs, indicating a loss of crystallinity and the formation of an amorphous phase. However, after the regeneration of the catalytic material, the XRD pattern was restored, displaying sharper and more defined reflections consistent with a material like the as-prepared catalyst. Further characterization of the regenerated material using HRTEM microscopy confirmed the disaggregation of NiNPs. The average particle size decreased from approximately 80 nm in the spent material to about 5 nm after regeneration (Fig. 13).

The recycling and regeneration studies reveal that **NiNPs/NHC@MXene** suffers from deactivation due to nanoparticle sintering. Importantly, this deactivation can be reversed through a mild, room-temperature reduction treatment effectively restoring both the nanoparticle dispersion and the catalytic activity. This approach highlights the potential of **NiNPs/NHC@MXene** as a sustainable and reusable catalytic system

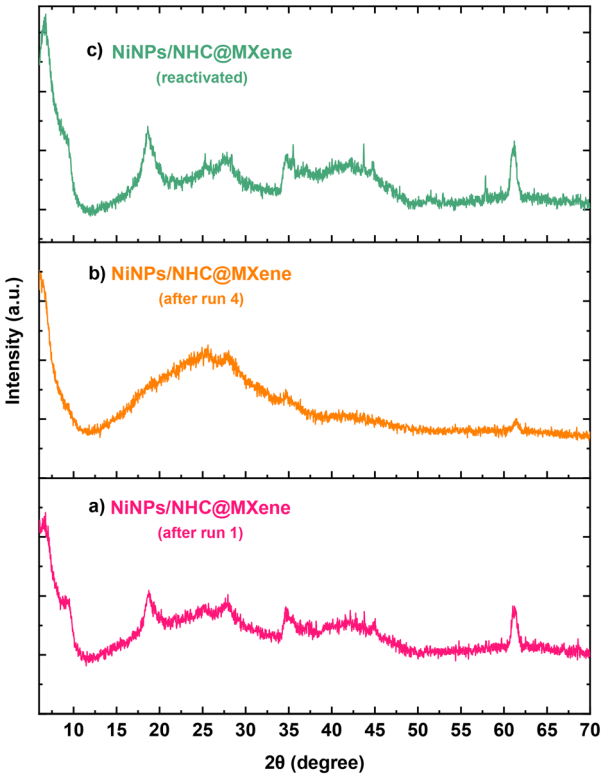

Fig. 12 XRD evolution of **NiNPs/NHC@MXene** during recycling and reusability experiments. XRD spectrum after run 1 (a), after run 4 (b) and after reactivation (c).

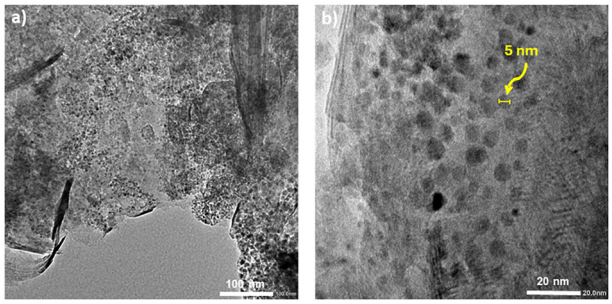

Fig. 13 HRTEM characterization of **NiNPs/NHC@MXene** after the regeneration procedure at 100 nm (a) and 20 nm (b).

whose performance is comparable to those of state-of-the-art nickel-based catalysts (Table S1).[49–56,79]

Conclusions

This study presents the development of a hybrid catalytic material consisting of nickel nanoparticles functionalized with NHC ligands and supported on **Ti_3C_2 MXene** (**NiNPs/NHC@MXene**). This material exhibits high catalytic efficiency and selectivity in the hydrogenation of quinolines, performing comparably to state-of-the-art nickel-based systems (Table S1). The role of the NHC ligand has been scrutinized, indicating the impact in the initial formation of metal nanoparticles on the material's surface by controlling the size and morphology.

A distinctive feature of the **NiNPs/NHC@MXene** catalyst is its broad substrate scope. Recycling experiments revealed a gradual decrease in catalytic performance over successive cycles, primarily attributed to nanoparticle growth and agglomeration due to ligand disappearance. Notably, this deactivation can be reversed: a mild regeneration treatment under reducing conditions using $^{t}BuNH_2{\cdot}BH_3$ successfully restores the catalytic activity to its original level.

The hydrogenation activity and regenerability of the **NiNPs/NHC@MXene** system exemplify a sustainable strategy for designing efficient catalysts based on Earth-abundant metals. Moreover, these results underscore the versatility of **Ti_3C2 MXene** as a suitable support for metal nanoparticles. Future efforts directed toward minimizing deactivation pathways and optimizing regeneration strategies will be crucial for extending catalyst lifetime and advancing the practical deployment of MXene-supported catalytic systems.

Author contributions

Judith Medina-Vargas, Santiago Martín and Iván Sorribes contributed to investigation, methodology, validation and data curation of results as well as writing – review and editing. Hermenegildo García and Jose A. Mata contributed to conceptualization, formal analysis, resources, writing original draft, writing – review and editing and funding acquisition. All authors have given approval to the final version of the manuscript.

Conflicts of interest

There are no conflicts to declare.

Data availability

The data supporting this article have been included as part of the supplementary information (SI). Supplementary information: additional characterization of materials by XPS, SEM and HRTEM. Further details of experimental procedures, NMR characterization of organic products and quantification analysis. See DOI: https://doi.org/10.1039/d5dt02759d.

Acknowledgements

Thanks to the Spanish Ministry of Science and Innovation for financial support through the projects PID2021-126071OB-C21, PID2021-126071OB-C22 and CEX2023-001286-S, funded by MICIN/AEI/10.13039/501100011033/FEDER "Una manera de hacer Europa". Generalitat Valenciana (MFA/2022/043) with funding from European Union NextGenerationEU

and Universitat Jaume I (UJI-B2022-23 and GACUJIMB/2023/13) is also gratefully acknowledged. I. S. thanks the Grant CNS2022-136183 funded by MICIU/AEI/10.13039/501100011033 and by "European Union NextGenerationEU/PRTR", and the Grant PID2022-143164OA-I00 funded by MICIU/AEI/10.13039/501100011033 and by "ERDF/EU". I.S. also gratefully acknowledges the program ESGENT from Generalitat valenciana (CIESGT/2024/16). J. M.-V. thanks the program "Santiago Grisolia" (GrisoliaP2021/114). The authors thank 'Servei Central d'Instrumentació Científica (SCIC) de la Universitat Jaume I'. S. M. is grateful to Gobierno de Aragón for the grant E31_23R with European Social Funds (Construyendo Europa desde Aragón).

References

1 D. Astruc, *Nanoparticles and Catalysis*, Wiley-VCH Verlag GmbH & Co. KGaA, Weinheim, Germany, 2007.
2 N.-D. Jaji, H. L. Lee, M. H. Hussin, H. M. Akil, M. R. Zakaria and M. B. H. Othman, Advanced nickel nanoparticles technology: From synthesis to applications, *Nanotechnol. Rev.*, 2020, **9**, 1456–1480.
3 F. e Silva, V. Salim and T. Rodrigues, Controlled Nickel Nanoparticles: A Review on How Parameters of Synthesis Can Modulate Their Features and Properties, *AppliedChem*, 2024, **4**, 86–106.
4 M. R. Ahghari, V. Soltaninejad and A. Maleki, Synthesis of nickel nanoparticles by a green and convenient method as a magnetic mirror with antibacterial activities, *Sci. Rep.*, 2020, **10**, 12627.
5 Z. Ji, X. Shen, G. Zhu, H. Zhou and A. Yuan, Reduced graphene oxide/nickel nanocomposites: facile synthesis, magnetic and catalytic properties, *J. Mater. Chem.*, 2012, **22**, 3471–3477.
6 M. G. Avello, S. Golling, L. Truong-Phuoc, L. Vidal, T. Romero, V. Papaefthimiou, N. Gruber, M. J. Chetcuti, F. R. Leroux, M. Donnard, V. Ritleng, C. Pham-Huu and C. Michon, (NHC-olefin)-nickel(0) nanoparticles as catalysts for the (Z)-selective semi-hydrogenation of alkynes and ynamides, *Chem. Commun.*, 2023, **59**, 1537–1540.
7 P. Ryabchuk, A. Agapova, C. Kreyenschulte, H. Lund, H. Junge, K. Junge and M. Beller, Heterogeneous nickel-catalysed reversible, acceptorless dehydrogenation of N-heterocycles for hydrogen storage, *Chem. Commun.*, 2019, **55**, 4969–4972.
8 M. D. de los Bernardos, S. Pérez-Rodríguez, A. Gual, C. Claver and C. Godard, Facile synthesis of NHC-stabilized Ni nanoparticles and their catalytic application in the Z-selective hydrogenation of alkynes, *Chem. Commun.*, 2017, **53**, 7894–7897.
9 J.-F. Soulé, H. Miyamura and S. Kobayashi, Copolymer-Incarcerated Nickel Nanoparticles with N -Heterocyclic Carbene Precursors as Active Cross-Linking Agents for Corriu–Kumada–Tamao Reaction, *J. Am. Chem. Soc.*, 2013, **135**, 10602–10605.
10 F. Alonso, P. Riente and M. Yus, Alcohols for the α–Alkylation of Methyl Ketones and Indirect Aza–Wittig Reaction Promoted by Nickel Nanoparticles, *Eur. J. Org. Chem.*, 2008, **2008**, 4908–4914.
11 A. Charvieux, J. B. Giorgi, N. Duguet and E. Métay, Solvent-free direct α-alkylation of ketones by alcohols catalyzed by nickel supported on silica–alumina, *Green Chem.*, 2018, **20**, 4210–4216.
12 D. Bouzouita, J. M. Asensio, V. Pfeifer, A. Palazzolo, P. Lecante, G. Pieters, S. Feuillastre, S. Tricard and B. Chaudret, Chemoselective H/D exchange catalyzed by nickel nanoparticles stabilized by N-heterocyclic carbene ligands, *Nanoscale*, 2020, **12**, 15736–15742.
13 G. Wu, C. Zhang, S. Li, Z. Han, T. Wang, X. Ma and J. Gong, Hydrogen Production via Glycerol Steam Reforming over Ni/Al_2O_3: Influence of Nickel Precursors, *ACS Sustainable Chem. Eng.*, 2013, **1**, 1052–1062.
14 S. Chen, J. Duan, J. Ran, M. Jaroniec and S. Z. Qiao, N-doped graphene film-confined nickel nanoparticles as a highly efficient three-dimensional oxygen evolution electrocatalyst, *Energy Environ. Sci.*, 2013, **6**, 3693–3699.
15 L. Gu, C. Zhang, Y. Guo, J. Gao, Y. Yu and B. Zhang, Enhancing Electrocatalytic Water Splitting Activities via Photothermal Effect over Bifunctional Nickel/Reduced Graphene Oxide Nanosheets, *ACS Sustainable Chem. Eng.*, 2019, **7**, 3710–3714.
16 D. D. Kruger, J. J. Delgado, F. J. Recio, S. Goberna-Ferrón, A. Primo and H. García, Influence of surface terminal groups on the efficiency of two-electron oxygen reduction reaction catalyzed by iron single atoms on $Ti_3C_2T_x$ (T = Cl, Br, NH) MXene, *J. Mater. Chem. A*, 2024, **12**, 25291–25303.
17 S. Ghosh, S. Gupta, M. Gregoire, T. Ourlin, P.-F. Fazzini, E. Abi-Aad, C. Poupin and B. Chaudret, Catalytic Sabatier Process under Thermally and Magnetically Induced Heating: A Comparative Case Study for Titania-Supported Nickel Catalyst, *Nanomaterials*, 2023, **13**, 1474.
18 S. Navalon, A. Dhakshinamoorthy, M. Alvaro and H. Garcia, Metal nanoparticles supported on two-dimensional graphenes as heterogeneous catalysts, *Coord. Chem. Rev.*, 2016, **312**, 99–148.
19 D. Skoda, J. Vilcakova, R. S. Yadav, B. Hanulikova, T. Capkova, M. Jurca, M. Urbanek, P. Machac, L. Simonikova, J. Antos and I. Kuritka, Nickel nanoparticle–decorated reduced graphene oxide via one-step microwave-assisted synthesis and its lightweight and flexible composite with Polystyrene-block-poly(ethylene-ran-butylene)-block-polystyrene polymer for electromagnetic wave shielding application, *Adv. Compos. Hybrid Mater.*, 2023, **6**, 113.
20 P. Lara, O. Rivada-Wheelaghan, S. Conejero, R. Poteau, K. Philippot and B. Chaudret, Ruthenium Nanoparticles Stabilized by N-Heterocyclic Carbenes: Ligand Location and Influence on Reactivity, *Angew. Chem., Int. Ed.*, 2011, **50**, 12080–12084.
21 C. Pan, K. Pelzer, K. Philippot, B. Chaudret, F. Dassenoy, P. Lecante and M.-J. Casanove, Ligand-Stabilized

Ruthenium Nanoparticles: Synthesis, Organization, and Dynamics, *J. Am. Chem. Soc.*, 2001, **123**, 7584–7593.

22 A. García-Zaragoza, C. Cerezo-Navarrete, A. Mollar-Cuni, P. Oña-Burgos, J. A. Mata, A. Corma and L. M. Martínez-Prieto, Tailoring graphene-supported Ru nanoparticles by functionalization with pyrene-tagged N-heterocyclic carbenes, *Catal. Sci. Technol.*, 2022, **12**, 1257–1270.

23 C. Copéret, A. Comas-Vives, M. P. Conley, D. P. Estes, A. Fedorov, V. Mougel, H. Nagae, F. Núñez-Zarur and P. A. Zhizhko, Surface Organometallic and Coordination Chemistry toward Single-Site Heterogeneous Catalysts: Strategies, Methods, Structures, and Activities, *Chem. Rev.*, 2016, **116**, 323–421.

24 L. Shen, J. Xu, M. Zhu and Y.-F. Han, Essential Role of the Support for Nickel-Based CO 2 Methanation Catalysts, *ACS Catal.*, 2020, **10**, 14581–14591.

25 J. Wang, M. Zhang, T. Miao, Y. Ling, Q. Wen, J. Zheng, J. Xu, T. Hayat and N. S. Alharbi, A facile self-template and carbonization strategy to fabricate nickel nanoparticle supporting N-doped carbon microtubes, *Inorg. Chem. Front.*, 2018, **5**, 844–852.

26 R. J. White, R. Luque, V. L. Budarin, J. H. Clark and D. J. Macquarrie, Supported metal nanoparticles on porous materials. Methods and applications, *Chem. Soc. Rev.*, 2009, **38**, 481–494.

27 C. Copéret, Single-Sites and Nanoparticles at Tailored Interfaces Prepared via Surface Organometallic Chemistry from Thermolytic Molecular Precursors, *Acc. Chem. Res.*, 2019, **52**, 1697–1708.

28 M. Babucci, A. Guntida and B. C. Gates, Atomically Dispersed Metals on Well-Defined Supports including Zeolites and Metal–Organic Frameworks: Structure, Bonding, Reactivity, and Catalysis, *Chem. Rev.*, 2020, **120**, 11956–11985.

29 M. Naguib, M. W. Barsoum and Y. Gogotsi, Ten Years of Progress in the Synthesis and Development of MXenes, *Adv. Mater.*, 2021, **33**, 202103393.

30 N. Kitchamsetti and A. L. F. de Barros, Recent Advances in MXenes Based Composites as Photocatalysts: Synthesis, Properties and Photocatalytic Removal of Organic Contaminants from Wastewater, *ChemCatChem*, 2023, **15**, e202300690.

31 V. Kamysbayev, A. S. Filatov, H. Hu, X. Rui, F. Lagunas, D. Wang, R. F. Klie and D. V. Talapin, Covalent surface modifications and superconductivity of two-dimensional metal carbide MXenes, *Science*, 2020, **369**, 979–983.

32 B. Anasori, M. R. Lukatskaya and Y. Gogotsi, 2D metal carbides and nitrides (MXenes) for energy storage, *Nat. Rev. Mater.*, 2017, **2**, 16098.

33 A. Ebadi Amooghin, A. Arabi Shamsabadi, M. M. Moftakhari Sharifzadeh, A. Salehi, H. Sanaeepur, M. Dadashi Firouzjaei, V. Rad, H. Jafarian, M. A. Elliott and H. Garcia, Tailoring MXene composition and structure for High-Performance mixed matrix membranes in CO2 separation applications, *Sep. Purif. Technol.*, 2025, **371**, 133360.

34 Z. Li, L. Yu, C. Milligan, T. Ma, L. Zhou, Y. Cui, Z. Qi, N. Libretto, B. Xu, J. Luo, E. Shi, Z. Wu, H. Xin, W. N. Delgass, J. T. Miller and Y. Wu, Two-dimensional transition metal carbides as supports for tuning the chemistry of catalytic nanoparticles, *Nat. Commun.*, 2018, **9**, 5258.

35 Z. Li and Y. Wu, 2D Early Transition Metal Carbides (MXenes) for Catalysis, *Small*, 2019, **15**, 1804736.

36 T. K. Slot, V. Natu, E. V. Ramos-Fernandez, A. Sepúlveda-Escribano, M. Barsoum, G. Rothenberg and N. R. Shiju, Enhancing catalytic epoxide ring-opening selectivity using surface-modified Ti 3 C 2 T x MXenes, *2D Mater.*, 2021, **8**, 035003.

37 J. D. Gouveia, Á. Morales-García, F. Viñes, F. Illas and J. R. B. Gomes, MXenes as promising catalysts for water dissociation, *Appl. Catal., B*, 2020, **260**, 118191.

38 N. Li, X. Chen, W.-J. Ong, D. R. MacFarlane, X. Zhao, A. K. Cheetham and C. Sun, Understanding of Electrochemical Mechanisms for CO $_2$ Capture and Conversion into Hydrocarbon Fuels in Transition-Metal Carbides (MXenes), *ACS Nano*, 2017, **11**, 10825–10833.

39 X. Zhang, C. Wu, Z. Shi, N. Wang and Y. Niu, Ni nanoparticles/NiFe LDHs/MXene ternary composites for catalytic hydrogenation of p-Nitrophenol, *Chem. Phys. Lett.*, 2025, **866**, 141931.

40 M. Bhosale, S. Thangarasu, N. Murugan, Y. A. Kim and T. Oh, Ti–MXene/α–Ni(OH) 2 Nanostructures as High–Performance Electrocatalyst for Oxygen Evolution Reaction, *ChemSusChem*, 2025, **18**, e202402603.

41 M. Smirnova, B. Scheibe, R. Ramírez-Grau, H. García and A. Lewandowska-Andralojc, Synergistic effects of MXene support and cobalt salts in dye-sensitized photocatalytic hydrogen generation, *Int. J. Hydrogen Energy*, 2024, **88**, 1098–1107.

42 A. Dhakshinamoorthy, R. Ramírez-Grau, H. Garcia and A. Primo, Opportunities of MXenes in Heterogeneous Catalysis: V2C as Aerobic Oxidation Catalyst, *Chem. – Eur. J.*, 2024, **30**, e202400576.

43 M. Puche, L. Liu, P. Concepción, I. Sorribes and A. Corma, Tuning the Catalytic Performance of Cobalt Nanoparticles by Tungsten Doping for Efficient and Selective Hydrogenation of Quinolines under Mild Conditions, *ACS Catal.*, 2021, **11**, 8197–8210.

44 I. Sorribes, L. Liu, A. Doménech-Carbó and A. Corma, Nanolayered Cobalt–Molybdenum Sulfides as Highly Chemo- and Regioselective Catalysts for the Hydrogenation of Quinoline Derivatives, *ACS Catal.*, 2018, **8**, 4545–4557.

45 A. Mollar-Cuni, S. Martín, G. Guisado-Barrios and J. A. Mata, Dual role of graphene as support of ligand-stabilized palladium nanoparticles and carbocatalyst for (de)hydrogenation of N-heterocycles, *Carbon*, 2023, **206**, 314–324.

46 D. Teichmann, W. Arlt and P. Wasserscheid, Liquid Organic Hydrogen Carriers as an efficient vector for the transport and storage of renewable energy, *Int. J. Hydrogen Energy*, 2012, **37**, 18118–18132.

47 D. Teichmann, W. Arlt, P. Wasserscheid and R. Freymann, A future energy supply based on Liquid Organic Hydrogen Carriers (LOHC), *Energy Environ. Sci.*, 2011, **4**, 2767–2773.

48 A. F. Dalebrook, W. Gan, M. Grasemann, S. Moret and G. Laurenczy, Hydrogen storage: beyond conventional methods, *Chem. Commun.*, 2013, **49**, 8735–8751.
49 V. Vermaak, H. C. M. Vosloo and A. J. Swarts, Fast and Efficient Nickel(II)–catalysed Transfer Hydrogenation of Quinolines with Ammonia Borane, *Adv. Synth. Catal.*, 2020, **362**, 5788–5793.
50 R. Yun, W. Ma, L. Hong, Y. Hu, F. Zhan, S. Liu and B. Zheng, Ni@PC as a stabilized catalyst toward the efficient hydrogenation of quinoline at ambient temperature, *Catal. Sci. Technol.*, 2019, **9**, 6669–6672.
51 L. Niu, Y. An, X. Yang, G. Bian, Q. Wu, Z. Xia and G. Bai, Highly dispersed Ni nanoparticles encapsulated in hollow mesoporous silica spheres as an efficient catalyst for quinoline hydrogenation, *Mol. Catal.*, 2021, **514**, 111855.
52 V. Goyal, T. Bhatt, A. Kuttasseri, A. Mahata, R. Zbořil, K. Natte and R. V. Jagadeesh, A biomass-derived nickel-based nanomaterial as a sustainable and reusable catalyst for hydrogenation of arenes and heteroarenes, *RSC Sustainability*, 2025, **3**, 2235–2245.
53 Z. Yuan, X. Li, G. Wang, Z. Zhu, Y. Liao, Z. Zhang and B. Liu, Efficient hydrogenation of N-heteroarenes into N-heterocycles over MOF-derived CeO_2 supported nickel nanoparticles, *Mol. Catal.*, 2023, **540**, 113052.
54 P. Ryabchuk, G. Agostini, M.-M. Pohl, H. Lund, A. Agapova, H. Junge, K. Junge and M. Beller, Intermetallic nickel silicide nanocatalyst—A non-noble metal–based general hydrogenation catalyst, *Sci. Adv.*, 2018, **4**, eaat0761.
55 S. Mao, P. Ryabchuk, S. Dastgir, M. Anwar, K. Junge and M. Beller, Silicon-Enriched Nickel Nanoparticles for Hydrogenation of N-Heterocycles in Aqueous Media, *ACS Appl. Nano Mater.*, 2022, **5**, 5625–5630.
56 Y. Hu, M. Liu, S. Bartling, H. Lund, H. Atia, P. J. Dyson, M. Beller and R. V. Jagadeesh, A general and robust Ni-based nanocatalyst for selective hydrogenation reactions at low temperature and pressure, *Sci. Adv.*, 2023, **9**, eadj8225.
57 S. Sabater, J. A. Mata and E. Peris, Catalyst enhancement and recyclability by immobilization of metal complexes onto graphene surface by noncovalent interactions, *ACS Catal.*, 2014, **4**, 2038–2047.
58 J. Medina-Vargas, A. Mollar-Cuni, S. Martín, I. Sorribes and J. A. Mata, Graphene as a Suitable Support for Nickel Nanoparticles Functionalized with NHC Ligands in Dehydrogenation of Alcohols, *ChemCatChem*, 2025, **17**, e202500490.
59 M. Naguib, M. Kurtoglu, V. Presser, J. Lu, J. Niu, M. Heon, L. Hultman, Y. Gogotsi and M. W. Barsoum, Two–Dimensional Nanocrystals Produced by Exfoliation of Ti_3AlC_2, *Adv. Mater.*, 2011, **23**, 4248–4253.
60 M. Alhabeb, K. Maleski, B. Anasori, P. Lelyukh, L. Clark, S. Sin and Y. Gogotsi, Guidelines for Synthesis and Processing of Two-Dimensional Titanium Carbide (Ti3C2Tx MXene), *Chem. Mater.*, 2017, **29**, 7633–7644.
61 D. Ventura-Espinosa, A. Carretero-Cerdán, M. Baya, H. García and J. A. Mata, Catalytic Dehydrogenative Coupling of Hydrosilanes with Alcohols for the Production of Hydrogen On-demand: Application of a Silane/Alcohol Pair as a Liquid Organic Hydrogen Carrier, *Chem. – Eur. J.*, 2017, **23**, 10815–10821.
62 D. Ventura-Espinosa, S. Sabater, A. Carretero-Cerdán, M. Baya and J. A. Mata, High Production of Hydrogen on Demand from Silanes Catalyzed by Iridium Complexes as a Versatile Hydrogen Storage System, *ACS Catal.*, 2018, **8**, 2558–2566.
63 A. Mollar-Cuni, P. Borja, S. Martin, G. Guisado-Barrios and J. A. Mata, A Platinum Molecular Complex Immobilised on the Surface of Graphene as Active Catalyst in Alkyne Hydrosilylation, *Eur. J. Inorg. Chem.*, 2020, **2020**, 4254–4262.
64 A. Mollar-Cuni, D. Ventura-Espinosa, S. Martín, Á. Mayoral, P. Borja and J. A. Mata, Stabilization of Nanoparticles Produced by Hydrogenation of Palladium-N-Heterocyclic Carbene Complexes on the Surface of Graphene and Implications in Catalysis, *ACS Omega*, 2018, **3**, 15217–15228.
65 D. Ventura-Espinosa, S. Martín, H. García and J. A. Mata, Ligand effects in the stabilization of gold nanoparticles anchored on the surface of graphene: Implications in catalysis, *J. Catal.*, 2021, **394**, 113–120.
66 D. Ventura-Espinosa, S. Sabater and J. A. Mata, Enhancement of gold catalytic activity and stability by immobilization on the surface of graphene, *J. Catal.*, 2017, **352**, 498–504.
67 S. M. M. Raj, A. K. Sundramoorthy, R. Atchudan, D. Ganapathy and A. Khosla, Review—Recent Trends on the Synthesis and Different Characterization Tools for MXenes and their Emerging Applications, *J. Electrochem. Soc.*, 2022, **169**, 077501.
68 Y. Cao, Q. Deng, Z. Liu, D. Shen, T. Wang, Q. Huang, S. Du, N. Jiang, C.-T. Lin and J. Yu, Enhanced thermal properties of poly(vinylidene fluoride) composites with ultrathin nanosheets of MXene, *RSC Adv.*, 2017, **7**, 20494–20501.
69 L.-Å. Näslund, P. O. Å. Persson and J. Rosen, X-ray Photoelectron Spectroscopy of Ti_3AlC_2, $Ti_3C_2T_z$, and TiC Provides Evidence for the Electrostatic Interaction between Laminated Layers in MAX-Phase Materials, *J. Phys. Chem. C*, 2020, **124**, 27732–27742.
70 M. Mičušík, M. Šlouf, A. Stepura, Y. Soyka, E. Ovodok, M. Procházka and M. Omastová, Aging of 2D MXene nanoparticles in air: An XPS and TEM study, *Appl. Surf. Sci.*, 2023, **610**, 155351.
71 R. Ramírez-Grau, P. Garcia-Aznar, G. Sastre, S. Gobena-Ferrón, O. Pavel, A. Tirsoaga, B. Cojocaru, D. G. Popescu, V. I. Parvulescu, A. Primo and H. García, MXenes as Heterogeneous Thermal Catalysts: Regioselective Anti-Markovnikov Hydroamination of Terminal Alkynes with 10^2 h^{-1} Turnover Frequencies, *J. Am. Chem. Soc.*, 2025, **147**, 3315–3332.
72 B. B. Nayak, S. Vitta, A. K. Nigam and D. Bahadur, Ni and Ni–nickel oxide nanoparticles with different shapes and a core–shell structure, *Thin Solid Films*, 2006, **505**, 109–112.

73 P. Song, D. Wen, Z. X. Guo and T. Korakianitis, Oxidation investigation of nickel nanoparticles, *Phys. Chem. Chem. Phys.*, 2008, **10**, 5057–5065.
74 V. Vonk, N. Khorshidi and A. Stierle, Structure and Oxidation Behavior of Nickel Nanoparticles Supported by YSZ(111), *J. Phys. Chem. C*, 2017, **121**, 2798–2806.
75 J. Wang, Y. Wang, Y. Wang, X. Li, C. Wu, T. Zhang, B. Tian, L. Qian, Y. Guo, L. Wu, L. Zheng, Y. Li and X. Ding, Novel two-dimensional Ti3C2Tx MXene-supported Ni-M (M = Pd, Pt, Ru): A remarkable catalyst for efficient HDO of guaiacol under hydrothermal conditions: Performance, mechanism and kinetic studies, *Fuel*, 2024, **374**, 132493.
76 S. Qiu, Q. Zhang, W. Lv, T. Wang, Q. Zhang and L. Ma, Simply packaging Ni nanoparticles inside SBA-15 channels by co-impregnation for dry reforming of methane, *RSC Adv.*, 2017, **7**, 24551–24560.
77 J. Gao, Y. Cao, G. Luo, J. Fan, J. H. Clark and S. Zhang, High-efficiency catalytic hydrodeoxygenation of lignin-derived vanillin with nickel-supported metal phosphate catalysts, *Chem. Eng. J.*, 2022, **448**, 137723.
78 J. Zhou, Y. Zhang, S. Li and J. Chen, Ni/NiO Nanocomposites with Rich Oxygen Vacancies as High-Performance Catalysts for Nitrophenol Hydrogenation, *Catalysts*, 2019, **9**, 944.
79 D. Ren, L. He, L. Yu, R.-S. Ding, Y.-M. Liu, Y. Cao, H.-Y. He and K.-N. Fan, An Unusual Chemoselective Hydrogenation of Quinoline Compounds Using Supported Gold Catalysts, *J. Am. Chem. Soc.*, 2012, **134**, 17592–17598.